Chem Soc Rev

Chemical vapour deposition of group-VIB metal dichalcogenide monolayers: engineered substrates from amorphous to single crystalline

Chemical vapour deposition of group-VIB metal dichalcogenide monolayers: engineered substrates from amorphous to single crystalline

Qingqing Ji,[a] Yu Zhang, [ab] Yanfeng Zhang *[ab] and Zhongfan Liu*[a]

[a] Center for Nanochemistry (CNC), Beijing National Laboratory for Molecular Sciences, College of Chemistry and Molecular Engineering, Academy for Advanced Interdisciplinary Studies, Peking University, Beijing 100871, People's Republic of China.

[b] Department of Materials Science and Engineering, College of Engineering, Peking University, Beijing 100871, People's Republic of China

E-mail: yanfengzhang@pku.edu.cn; zfliu@pku.edu.cn

Abstract: As structural analogues of graphene but with a sizeable band gap, monolayers of group-VIB transition metal dichalcogenides (MX_2, M=Mo, W; X=S, Se, Te, etc.) have emerged as the ideal two dimensional prototype for exploring fundamental issues in physics such as valley polarization, and for engineering a wide range of nanoelectronic, optoelectronic and photocatalytic applications. Recently, chemical vapour deposition (CVD) was introduced as a more efficient preparation method than traditional chemical or physical exfoliation options, and has allowed for the successful synthesis of large-area MX_2 monolayers possessing a large domain size, high thickness uniformity and continuity, and satisfactory crystal quality. This tutorial review therefore focuses on introducing the more recent advances in the CVD growth of MX_2 (MoS_2, WS_2, $MoS_{2(1-x)}Se_{2x}$ etc.) monolayers via the sulphurisation/decomposition of pre-deposited metal-based precursors, or the one-step reaction and deposition of gaseous metal and chalcogen feedstocks. Differences in growth behaviour caused by commonly used amorphous SiO_2/Si, and newly adopted insulating single crystal substrates such as sapphire, mica and $SrTiO_3$, are also comparatively presented. Also discussed are the essential parameters that influence the growth of MX_2, such as temperature, source-substrate distance and the composition of the carrier gas (Ar/H_2). Finally, an assessment is provided of viable future pathways for fine-tuning of the domain size and orientation, thickness uniformity, and bandgap of MX_2 and its alloys.
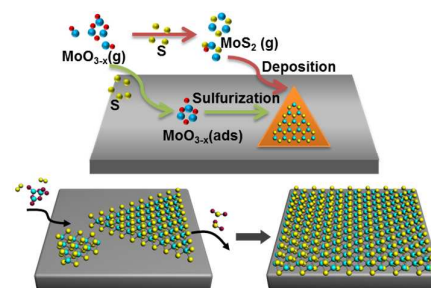
Key learning points:

1) Overview of the two main routes for synthesizing monolayer group-VIB metal dichalcogenides (MX_2) by chemical vapour deposition (CVD).

2) Summary of recent advances in the CVD synthesis of monolayer MX_2 on amorphous SiO_2/Si substrates.

3) Introduction of the CVD growth of monolayer MX_2 with engineered morphologies on some representative insulating single crystal substrates.

4) Assessment of the crystal quality of the CVD-synthesized monolayer MX_2.

5) Brief introduction of the CVD growth of monolayer MX_2 alloys.

Author biography

Zhongfan Liu received his PhD from the University of Tokyo in 1990. After a postdoctoral fellowship at Institute for Molecular Science (IMS), Japan, he became an associate professor (1993), full professor (1993) and Cheung Kong Chair professor (1999) of Peking University. He was elected as the member of Chinese Academy of Sciences (CAS) in 2011. He is now the directors of Institute of Physical Chemistry, Center for Nanoscale Science and Technology, and Center for Nanochemistry of Peking University. His research interest is focused on low dimensional carbon materials and novel 2D atomic crystals targeting nanoelectronic and energy conversion devices together with the exploration of fundamental phenomena in nanoscale systems.

Yanfeng Zhang received her PhD from the Institute of Physics in the Chinese Academy of Sciences in 2005. Later on, she worked as a JSPS fellow from 2006 to 2009 in Tohoku University, Japan. In 2010, she joined in the Center for Nanochemistry of Peking University, and the Department of Materials Science and Engineering in the College of Engineering of Peking University, and served as a research professor. Her research interests relate to the controlled growth, accurate characterization and novel property exploration of two dimensional atomic layer thin materials such as graphene, h-BN-graphene heterostructures, and transition metal dichalcogenides (TMDCs).

1 Introduction

As a new class of material, two-dimensional (2D) atomic crystals[1] have attracted enormous research interest in the last decade that has led to a number of breakthroughs in physics owing to the confined charge, spin and heat transport within the 2D planes. The most outstanding one of these materials is graphene, as its exceptional electronic, optical and mechanical properties[2] may hold great promise for a variety of future applications. However, the zero energy gap of graphene greatly impedes its application in logic electronics, creating a very real need for an analogous substitute that can offer a finite bandgap.

A significant advance in the 2D atomic-layer crystal field has been the recent rediscovery of transition metal dichalcogenides (TMDCs),[3] which have long been exploited as industrial lubricants. This resurgence has been largely driven by increasing research interest in group-VIB metal dichalcogenides (MX_2, M=Mo, W; X=S, Se, Te) with sizable bandgaps of around 1-2 eV. Similar with graphene, the constituent layers in MX_2 are covalently bonded in the 2D plane, but only weakly coupled with neighbouring layers through van der Waals (vdW) interaction. The remarkable properties of monolayer MX_2 can be exemplified by those of molybdenum disulphide (MoS_2). When bulk MoS_2 is thinned down to a monolayer, an indirect-to-direct bandgap transition occurs that is accompanied by a strong photoluminescent (PL) emission.[4] Meanwhile, the heavy atom nature of Mo contributes rich van Hove singularities to its density of states (DOS) spectrum, thereby facilitating a strong interaction with visible light[5] and a ~10 % absorption at sub-nanometre thicknesses.[6] The 2D confinement of photogenerated charge carriers has also made possible the formation of trions[7] that are both optically and electrically active, whilst the lack of inversion symmetry and strong spin-orbit coupling leads to a coupling of spin and valley physics. This means that carrier populations in distinct valleys can be controlled by optically exciting samples with a circularly polarized light, which may represent the first step toward a new field of valleytronics.[8] All these factors, combined with an appreciable charge mobility,[9] have made monolayer MoS_2 a promising candidate for investigating fundamental aspects of physics such as valley polarization and the multi-body interactions of carriers. In addition, it also presents a promising material for the design of a variety of unique practical devices in the fields of nanoelectronics, optoelectronics, photocatalysis, etc.

Traditionally, monolayer MX_2 is obtained via top-down methods, such as mechanical exfoliation,[1,4,9] chemical[10] and electrochemical exfoliation[11], and direct sonication in solvents,[12] to separate the stacked thick layers (or even bulk materials) of MX_2. Nevertheless, the resulted MX_2 layers are typically microscale flakes with poor uniformity in film thickness, ranging from monolayer to tens of layers. To improve on this, several bottom-up methods have been recently developed to synthesize large-area MX_2 thin layers directly onto SiO_2/Si substrates. This has included the sulphurisation of pre-deposited Mo[13] or Mo oxide[14] layers, the decomposition of thiomolybdates[15], and chemical vapour deposition (CVD)

through a gas-phase reaction of MoO_{3-x} and sulphur.[16] Certain insulating single-crystal substrates such as sapphire, mica and $SrTiO_3$ have also been proven to be effective in ensuring uniform MX_2 film growth, which is considered to be due to a combination of their relatively flat surface, interface lattice matching, and suitable interfacial binding strength.

In this tutorial review, we introduce the concept of CVD synthesis of monolayer MX_2 (MoS_2, WS_2, $MoS_{2(1-x)}Se_{2x}$, etc.) on both amorphous SiO_2/Si and insulating single crystal substrates via two main routes. We also discuss the effects of some essential growth parameters such as temperature, source-substrate distance and carrier gas composition (Ar/H_2) on the controlled growth of monolayer MX_2. Finally, we relate these parameters to the distinct growth results such as flake morphology evolution, domain size and coverage variation, and the alignment of individual domains, with a view to providing further insight into how to improve the quality of CVD-synthesized MX_2.

2. CVD synthesis: growth routes and experimental setup

The CVD synthesis of monolayer MoS_2 (Fig. 1a) has to date been performed by one of the following two routes. The first is regarded as a two-step growth route, in which Mo-based precursors are initially deposited and then sulphurised/decomposed into MoS_2 (Route 1).[13-15] The second is considered as a one-step growth, wherein gaseous Mo and S feedstocks are simultaneously introduced and react to form MoS_2 on a substrate (Route 2).[16-18] Either of these routes can conceivably be extrapolated to obtain all possible MX_2 layers (WS_2[19,20], $MoSe_2$[21,22], WSe_2[23], etc.) Notably, a reductive H_2 carrier gas was found to be effective in promoting the gas-phase reaction of metal oxides and selenium, with the formation of high-quality monolayer diselenide films possessing comparable domain size and carrier mobility to their disulphide conterparts.[22,23]

Initially, amorphous SiO_2 substrates were utilized for MX_2 growth due to their perfect compatibility with Si-based electronics.[13-16] However, more recent studies[20,23-25] have revealed that insulating single crystals such as quartz, mica and sapphire (Fig. 1b) can also be employed for growing high-quality MX_2. The advantage of using these single crystal substrates lies in their rather high thermal stability and chemical inertness, as well as their characteristic hexagonal surface arrangement. Their atomically flat surface may also potentially facilitate precursor migration during CVD, thereby improving the thickness uniformity of resulting MX_2 layers. Furthermore, it is also possible that they could enable vdW epitaxy of monolayer MX_2, especially considering the lattice registry effect between the overlayer and substrate (*e.g.* a(mica)/a(MoS_2) = ~$\sqrt{3}$, a(sapphire)/a(MoS_2) = ~1.5).

Meanwhile, there is a need to develop different growth recipes for disparate MX$_2$/substrate systems, that take into account such variables as the growth temperature and time, system pressure, metal (or metal oxide) and chalcogen precursors, etc. In doing so, the provided broad tunability of growth may allow for the morphology, thickness, domain size and crystal orientation of MX$_2$ layers to be selectively engineered for specific applications.

Fig. 1c depicts a typical experimental setup for the low-pressure chemical vapour deposition (LPCVD) synthesis of MX$_2$. This consists of a multi-temperature-zone furnace equipped with a quartz tube, an upstream heating belt for the evaporation of chalcogen powders, and a cold trap for solidification of reactive species in the outflow. A mechanical pump is installed downstream to exhaust the outflow and maintain the low pressure of the growth system. If we consider the direct reaction of gaseous Mo and S feedstocks (Route 2) as an example, then the process can be described as follows. Firstly, a precursor MoO$_3$ powder and a suitable growth substrate are placed in upstream and downstream locations, respectively. The MoO$_3$ is then partially reduced by sulphur vapour to form a volatile MoO$_{3-x}$ species, which is subsequently conveyed downstream by the carrier gas and reacts with sulphur to deposit MoS$_2$ on the substrate.

The partial pressure of the reactive gaseous species can be fine-tuned by controlling the evaporation temperature of S and MoO$_3$, which can influence the subsequent adsorption and surface-bound reaction on the substrate. According to the ternary Mo-O-S phase diagram (Fig. 1d), too weak a reducing atmosphere (i.e. one that is sulphur-poor) should result in low-valence-state oxide or oxisulphide nanoparticles, thus preventing the formation of MoS$_2$ entirely.[26] On the other hand, an excess of sulphur may suppress the volatilization of MoO$_3$ by forming non-volatile species, again yielding little to no MoS$_2$ on the target substrate. Meanwhile, a high sulphurisation rate (corresponding to a high S partial pressure) could encapsulate MoO$_{3-x}$ nanoparticles with MoS$_2$ layers, thereby leading to the formation of MoS$_2$ inorganic fullerenes.[27] In light of this, a moderate sulphurisation rate (i.e. a suitable S partial pressure) is highly desirable to ensure 2D growth of MoS$_2$.

Although the growth dynamics of MoO$_{3-x}$ and S are still not fully understood, there are two possible channels for the surface growth that can be expected: (1) MoO$_{3-x}$ species adsorb and diffuse on the substrate, reacting with S to form MoS$_2$ (green arrows in Fig. 1e); (2) MoO$_{3-x}$ and S react directly in the gas phase, and the resulting MoS$_2$ clusters adsorb, nucleate, and grow on the substrate (red arrows in Fig. 1e). Clearly, these two channels are in direct competition and involve multiple elementary processes that cannot be separately controlled. Nevertheless, carefully controlling the substrate temperature should adjust the adsorption/desorption of both MoO$_{3-x}$ and MoS$_2$ clusters, and hence the nucleation density and domain size of the MoS$_2$ flakes. In this case, the evaporation temperature of the precursors, the substrate temperature and the precursor-substrate distance would all influence the final growth results.
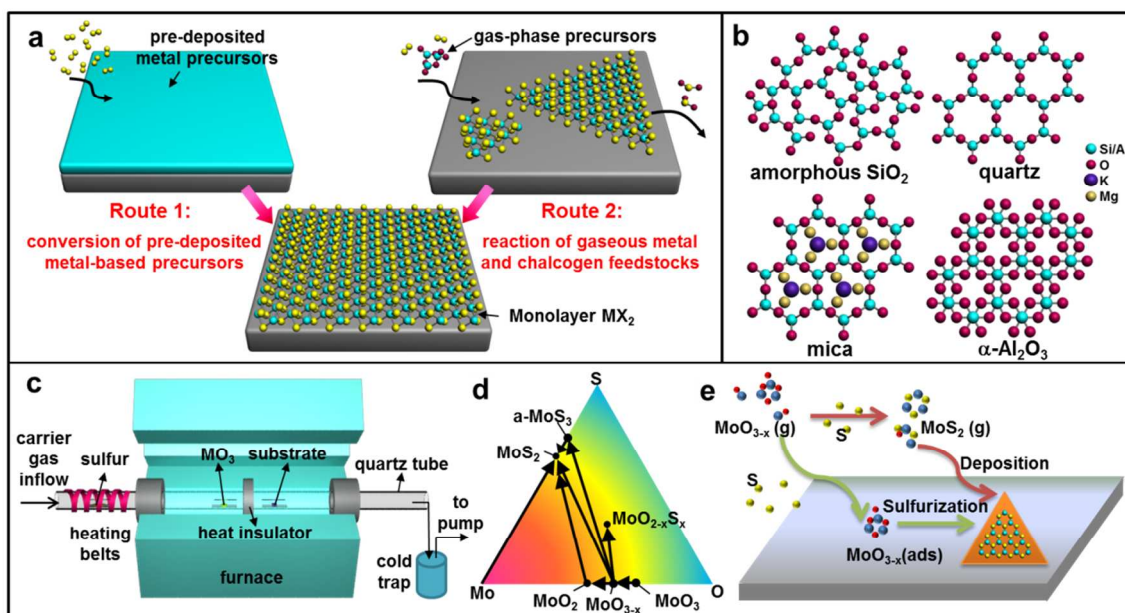
Fig. 1 General introduction to the CVD synthesis of MX$_2$ thin layers. (a) Two routes for MX$_2$ synthesis. (b) Commonly used insulating substrates for MX$_2$ growth (top view). (c) Typical setup of LPCVD system. (d) Mo-O-S ternary phase diagram, in which the labelled arrows indicate reaction pathways for the CVD growth of MoS$_2$ from MoO$_3$ precursors. (e) Possible growth processes of MoS$_2$ by the reaction of MoO$_{3-x}$ and S.

2.1 MX$_2$ synthesis *via* Route 1

In an early attempt reported by Lou et al., Mo layers measuring several nanometres in thickness were successfully deposited on SiO$_2$/Si substrates via e-beam evaporation, and then vapour-phase sulphurised in the CVD system.[13] This growth process represents the origin of MoS$_2$ synthesis via Route 1 (Fig. 2a), namely the sulphurisation/decomposition of pre-deposited Mo-based precursors. In this way, large-area MoS$_2$ with only a few layers in thickness have been synthesized, with the sample size only limited by the size of the growth substrate. However, owing to the high melting point (2610 °C) of Mo, the migration of Mo atoms is considered to be effectively suppressed at growth temperatures of ~750 °C, beyond which polycrystalline MoS$_2$ layers inevitably form. Although bright-field (BF) transmission electron microscopy (TEM) characterisation of the transferred MoS$_2$ film usually shows a uniform contrast (Fig. 2b), the corresponding selective area electron diffraction (SAED) pattern reveals multigroup, sixfold-symmetry spots (Fig. 2c). Furthermore, dark-field (DF) images of this area show evidence of disordered domains with an average size of ~20 nm (Fig. 2d). In the case of the few-layer MoS$_2$ films with high-density grain boundaries, a relatively low carrier mobility (0.004~0.04 cm^{2}V^{-1}s^{-1}) has been achieved. Consequently, Mo-based precursors with a low evaporation temperature are preferable in terms of improving the domain size and thickness uniformity of MoS$_2$ layers.

Molybdenum trioxide (MoO$_3$) was selected by Li et al. as an alternative precursor for MoS$_2$ growth on the basis of it having an evaporation temperature of ~700 °C.[28] With the aid of a thermal evaporator, it was readily deposited onto c-face sapphire substrates, forming a uniformly thin layer suitable for sulphurisation. Using this synthesis method, wafer-scale MoS$_2$ thin films were successfully prepared on sapphire substrates, wherein the film thickness (2-3 layers) was found to rely on the amount of pre-deposited MoO$_3$. In another similar work, crystalline rhomboidal MoO$_2$ microplates, as opposed to amorphous MoO$_3$ layers, were evolved on SiO$_2$/Si substrates under a weak reducing atmosphere of sulphur at 650–850 °C.[14] These MoO$_2$ microplates were then sulphurised to MoS$_2$ at 850–950 °C, with the MoS$_2$ thickness easily controlled by changing the duration of annealing under a sulphur atmosphere (Fig. 2e). Peeling off of the MoS$_2$ layers with an average domain size of ~10 μm, was achieved by virtue of the relatively weak adhesion between the MoS$_2$ and the MoO$_2$ base (Figs. 2f,g). The resulting MoS$_2$ flakes consisting of only a few layers demonstrated a relatively high carrier mobility of 0.1–10 cm^{2}V^{-1}s^{-1}.

Ammonium thiomolybdate ((NH$_4$)$_2$MoS$_4$) was also utilized by Li *et al.* for MoS$_2$ synthesis as both a Mo and S source.[15] To achieve this, a suitable growth substrate was first immersed in (NH$_4$)$_2$MoS$_4$ solution to obtain a uniform coating, which was then annealed under an Ar/H$_2$ atmosphere at 500 °C to convert it to a MoS$_2$ thin film. This method has proven capable of producing large-area MoS$_2$ thin films with a uniform thickness of 2-3 layers, as demonstrated by the atomic force microscopy (AFM) image in Fig. 2i. Notably, high-temperature annealing at 1000 °C under a sulphur atmosphere can further improve the crystal quality of MoS$_2$, which is believed to be most likely due to a suppression of oxygen doping in the lattice. Moreover, MoS$_2$ samples annealed under an Ar+S atmosphere (Fig. 2j) exhibit a distinctly larger domain size than those annealed in pure Ar (Fig. 2k) (hundreds versus tens of nanometres). It is also worth mentioning here that sapphire appears to be a much better substrate for MoS$_2$ growth than SiO$_2$/Si, as MoS$_2$ films synthesized on sapphire present much better crystallinity than that on SiO$_2$/Si, as evidenced by the TEM results in Figs. 2l and 2m.

In short, MX$_2$ synthesis via Route 1 (i.e. the sulphurisation/decomposition of pre-deposited metal-based precursor layers) is an effective means of preparing large-area MX$_2$ thin layers; however, it is still difficult to obtain large-scale uniform monolayers of MX$_2$ using current growth regimes. This is considered to be the result of the uncontrollable nature of the metal-based precursor in terms of the amount and uniformity of its deposition, as well as its limited diffusion and inefficient sulphurisation on growth substrates. Moreover, the domains and domain boundaries of MX$_2$ films prepared by this route are usually quite abundant and complex in the sense that they have a relatively small domain size (from tens of nanometres to sub-micron) and irregular domain shapes. Addressing these problems therefore requires the development of more sophisticated synthesis methods/processes.
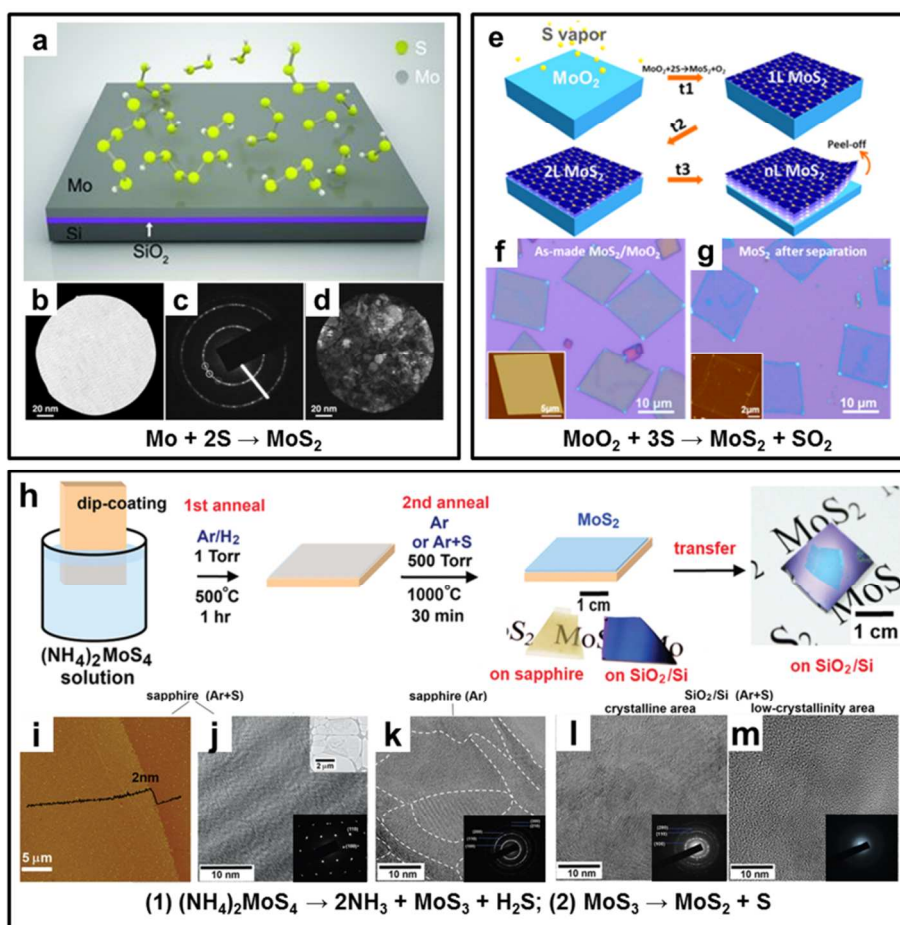
Fig. 2 Present synthesis systems following Route 1. (a) Schematic view of sulphurising a pre-deposited Mo layer to achieve MoS$_2$ thin films.[13] (b-d) Corresponding bright-field, SAED pattern, and dark-field TEM images, respectively, of the MoS$_2$ film in (a).[13] Reproduced with permission from Ref.13. Copyright 2012, John Wiley & Sons, Inc. (e) Layer-by-layer sulphurisation of pre-deposited MoO$_2$ flakes for the thickness-controllable synthesis of MoS$_2$.[14] (f) and (g) Optical images of as-made MoS$_2$/MoO$_2$ and peeled MoS$_2$ layers, respectively.[14] Reproduced with permission from Ref.14. Copyright 2013, American Chemical Society. (h) Synthesis of MoS$_2$ thin layers by the decomposition of thiomolybdates.[15] (i) AFM image of a MoS$_2$ trilayer grown on a sapphire substrate annealed in the presence of argon and sulphur (Ar + S).[15] (j) High-resolution TEM image of the MoS$_2$ trilayer.[15] (k) TEM image of MoS$_2$ grown on sapphire with Ar-only annealing.[15] (l, m) TEM images of a MoS$_2$ trilayer grown on a SiO$_2$/Si substrate annealed with Ar + S.[15] Reproduced with permission from Ref.15. Copyright 2012, American Chemical Society.

2.2 MX$_2$ synthesis *via* Route 2

A one-step growth route, namely the direct reaction of simultaneously introduced gaseous metal and chalcogen precursors (Route 2), has also been realized in CVD systems. In the initial experimental setup reported by Lin et al. (left panel of Fig. 3a), sulphur and MoO$_3$ powders were successively placed in the reaction chamber, with a SiO$_2$/Si substrate mounted face-down above the MoO$_3$.[16] Pre-treating this substrate by spin-casting graphene-like molecules (i.e. reduced graphene oxide, rGO) onto it was found to be preferable for inducing effective nucleation and layered growth of MoS$_2$; and the corresponding optical image shown in the right panel of Fig. 3a demonstrates the near triangular MoS$_2$ sheets of 1-3 layers that were obtained by this method. Further to this, Kong et al. used similar planar aromatic molecules as seeding promoters to grow MS$_2$ (M=Mo, W) on differently corrugated substrates (Fig. 3b) of quartz,

sapphire, Si particles, etc.[17] This same synthesis method was also utilized for fabricating vdW heterostructures of MX$_2$ on graphene and *h*-BN.[18] Notably, such one-step CVD produced regularly triangular shaped MoS$_2$ flakes presenting a typical domain size greater than 1 μm.

It was Lou et al. who were first to demonstrate that aromatic molecular seeds are not essential for initializing the layered growth of MoS$_2$, and achieved triangular monolayer MoS$_2$ flakes and their aggregates on bare SiO$_2$/Si substrates (Fig. 3c).[29] These sharp-edged triangular flakes with a typical edge length of ~10 μm were identified as single crystal domains on the basis of the fact that their SEAD patterns reveal only one set of diffraction spots. Moreover, the limiting factor for MoS$_2$ growth on bare SiO$_2$/Si was addressed to arise from a rare and complicated nucleation process (Figs. 3c and 3d),[29] wherein MoS$_2$ triangular domains and films are preferably

nucleated in the vicinity edges, scratches, dust particles, or rough areas. In light of this, patterned substrates with uniformly distributed rectangular SiO_2 micropillars were deliberately fabricated to promote MoS_2 nucleation and enable the growth of continuous MoS_2 films (Fig. 3e).[29] Nevertheless, the resulting films were found to actually be composed of randomly oriented domains, most likely mediated by the isotropic nature of the amorphous SiO_2 substrates. Thus, grain boundaries (GBs) typically occur at interfaces linking neighbouring grains, as is apparent in the high-resolution scanning transmission electron microscopy (STEM) images in Figs. 3f and 3g.[29]

Van der Zande et al. reported that polygonal MoS_2 flakes could be easily synthesized using an experimental setup similar to that shown in Fig. 3a. The optical image in Fig. 3h exhibits a monolayer MoS_2 polygon with a butterfly shape obtained by this method.[30] DF-TEM image of such a flake after transference onto a Cu grid

reveals two lobes of misoriented domains with a faceted tilt boundary (Figs. 3i and 3j) that confirms its polycrystalline nature. Moreover, it was found that adjacent MoS_2 grains sometimes overlap to form rotationally misaligned bilayer regions, which appear as regions of darker contrast in the BF-TEM image in Fig. 3k. This overlapping phenomenon has also been confirmed through DF-TEM (Fig. 3l)[30] and high-resolution STEM imaging.[29]

As mentioned earlier, the compatibility of SiO_2/Si with modern electronics makes it a popular substrate for growing MoS_2 monolayer and few layers with a relatively large domain size. However, in order to fully realize its practical application potential, it is necessary to further enlarge the size of single-crystalline MoS_2 domains whilst simultaneously preventing their overlap and ensuring an ordered orientation; requirements that would be difficult to achieve with amorphous SiO_2 substrates alone.
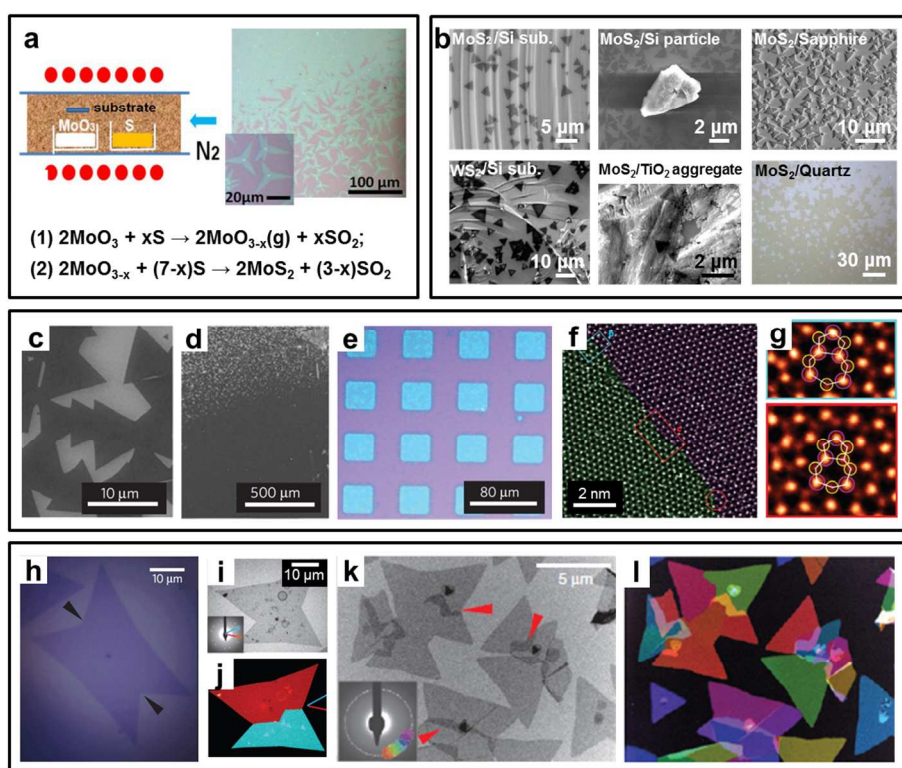
Fig. 3 Synthesis systems following Route 2. (a) Schematic illustration of an experimental setup (left), and an optical image of the MoS_2 flakes obtained by it (right).[16] Reproduced with permission from Ref.16. Copyright 2012, John Wiley & Sons, Inc. (b) Scanning electron microscope (SEM) images of MS_2 grown on various substrates using the setup shown in (a).[17] Reproduced with permission from Ref.17. Copyright 2013, American Chemical Society. (c) SEM images of sub-monolayer MoS_2 polycrystallites.[29] (d) SEM images showing the evolution of MoS_2 from sub-monolayer aggregates to a continuous film.[29] (e) Optical image of continuous MoS_2 monolayer growth on SiO_2/Si with pre-deposited SiO_2 patterns.[29] (f) Atomic-resolution image of a GB linking two misoriented domains.[29] (g) Atomic reconstruction at the GB.[29] Reproduced with permission from Ref.29. Copyright 2013, Nature Publishing Group. (h) Optical image of a MoS_2 polycrystalline flake with a butterfly shape.[30] (i, j) Bright-field and color-coded dark-field TEM images of a butterfly-shaped MoS_2 flake.[30] (k, l) Bright- and dark-field images of polycrystalline MoS_2 aggregates grown on SiO_2/Si.[30] Reproduced with permission from Ref.30. Copyright 2013, Nature Publishing Group.

Enlarging the size of single crystalline domains should be the main focus in improving MoS_2 growth to satisfy the requirements in practical device applications; and indeed, using ambient-pressure

CVD (APCVD), van der Zande et al. have achieved near-triangular MoS_2 flakes (Fig. 4a) with the longest edge length so far of ~120 μm (Fig. 4b).[30] DF-TEM image for such a concave-edged triangle flakes

(Fig. 4c) reveals nearly the same lattice orientation all over the flake, highly suggestive of a single crystal nature. Particularly, by virtue of the intensity maps for the SAED patterns, distinct edge terminations of Mo-zigzag (Figs. 4d-f) and S-zigzag (Fig. 4g) were confirmed for the sharp- and concave-edged triangular flakes, respectively.

The optimization of large-domain MoS_2 growth can be achieved by using carefully cleaned SiO_2/Si substrates and minimising exposure of the precursors to air during storage.[30] However, even with this, a wide grain size distribution and inhomogeneous inhabitation of MoS_2 nucleation centres still occurs in the growth system. This indicates that in addition to the substrate effect, MoS_2 growth is quite sensitive to the localised concentration of precursors, and thus a well-controlled concentration gradient should help achieve a more uniform nucleation on the substrate.

It is worth noting that most past examples of MoS_2 synthesis by CVD have adopted similar experimental setups to that shown in Fig. 3a, in which a SiO_2/Si substrate is placed face-down on a boat filled with MoO_3. Such a configuration is considered to create a superior local environment in terms of providing a high concentration of gaseous MoO_{3-x} precursors for MoS_2 growth. More recently, Yu et al. reported a revised setup in which a small quartz tube sealed at one end is used as the container for the precursors and the substrate (Fig. 4h). This method has proven to be effective in synthesizing triangular WS_2 monolayers with an edge length up to 178 μm (Fig.

4i);[31] and interestingly, a series of optical images were captured of WS_2 flakes at different growth stages showing the growth process (Fig. 4j). In this, thick WS_{2+x} triangle flakes are initially produced, the apexes of which then act as active nucleation sites. A sequence of intersecting few layer triangles grow successively at the apexes, eventually merging to form a large concave triangle.[31] With further heating under a sulphur atmosphere, this thick flake starts to expand and thin, and finally develops into a regular triangular monolayer. This suggests that even single-crystalline triangular flakes may not grow from just the one nucleus, but rather from an aggregation of triangular flakes.

In summary, although both Route 1 and Route 2 have proven effective for preparing large area MX_2 thin layers, it is the latter that has the greater potential for obtaining large-area, large-domain monolayers of MX_2 with a uniform thickness. This is considered to be a result of the well-controlled release of precursors using this method, as well as the more efficient sulphurisation in the gas phase and on the substrates. Furthermore, although SiO_2/Si is currently the preferred substrate for growing MX_2 thin layers, experimental evidence suggests that an amorphous SiO_2 surface is less effective in capturing the MoO_{3-x}/MoS_2 species needed to grow large-area monolayer MoS_2 films with satisfactory continuity and thickness uniformity; though this can be overcome to some extent by casting graphene-like seeds on the substrate or patterning it with SiO_2 micropillars.
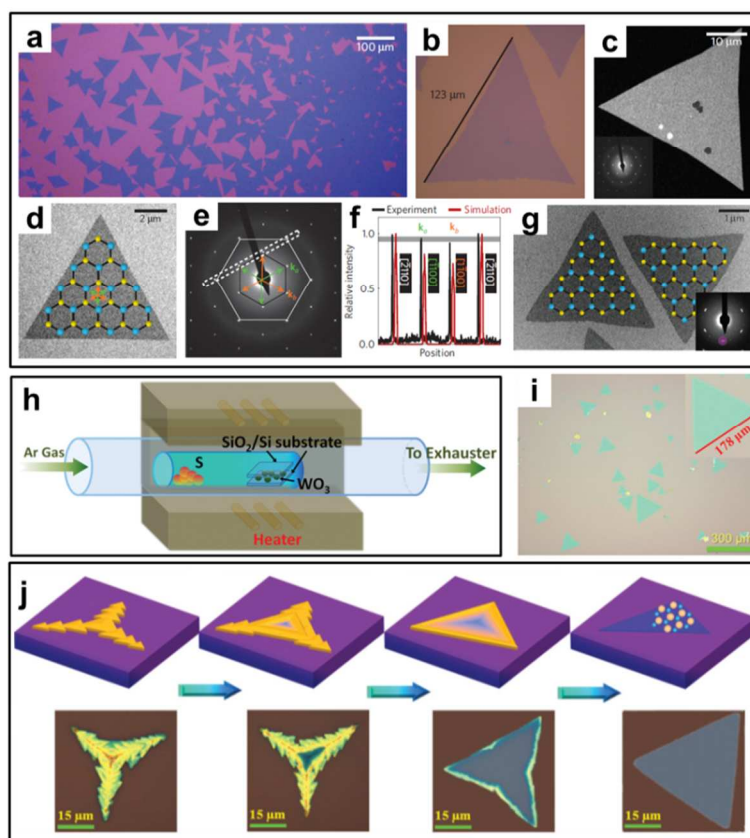
Fig. 4 Growth of large-domain MS_2 triangular single crystals. (a) Low-magnification optical images of CVD synthesized MoS_2 on SiO_2/Si.[30] (b) Close-up optical image of a triangular MoS_2 flake with an edge size of ~120 μm.[30] (c) DF-TEM image and (inset) corresponding SAED

pattern demonstrating the single crystallinity of the triangular flake.[30] (d) BF-TEM image of a single-crystal triangle with a Mo-zigzag edge orientation.[30] (e) Diffraction pattern from (d).[30] The asymmetry of the Mo and S sublattices separates the first-order diffraction spots into two families (k_a and k_b), as labelled in (e). (f) A line profile through experimentally measured diffraction spots (black) and Bloch-wave simulations (red).[30] The higher intensity k_a spots point towards the Mo sublattice, as indicated by the arrows in (d). (g) BF-TEM image of two triangles with S-zigzag edge orientations.[30] The curved crystal edges contrasts with the sharp crystal edges of the Mo-zigzag edges in (d). Reproduced with permission from Ref.30. Copyright 2013, Nature Publishing Group. (h) Experimental setup for growing large domain WS_2, in which sulphur and WO_3 powders are loaded into a quartz tube that is sealed at one end.[31] (i) Optical image of as-grown WS_2 flakes with a maximum edge length of 178 μm.[31] (j) Proposed mechanism for growing large-domain WS_2 triangles.[31] Reproduced with permission from Ref.31. Copyright 2014, John Wiley & Sons, Inc.

3. CVD on insulating single crystals

Insulating single crystals such as sapphire, mica and $SrTiO_3$ (STO) have been considered as more suitable substrates for the CVD growth of MX_2 based on their ultraflat surfaces, excellent thermal stability, and possible lattice registry with MX_2 adlayers. This section therefore discusses in detail the CVD growth of monolayer MX_2 on representative insulating single crystal substrates[20, 24, 34] and considers the effects of essential growth parameters such as temperature, precursor-substrate distance and the composition of the carrier gas (Ar/H$_2$). The aim here is to demonstrate the ways in which the growth process can be manipulated to control the compact flake shape, uniformity of domain orientation and thickness, crystal quality, etc.

3.1 Flake morphology engineering

Sapphire (0001) is a commonly used single crystal substrate in the epitaxy of various inorganic thin films, such as gallium nitride, magnesium boride, and diamond, due to its chemically inert surface and probable lattice matching with overlayer materials. As previously mentioned, this substrate has also been utilized in the growth of MoS_2 by decomposing thiomolybdates inside an APCVD system (Figs. 2h-k).[15] Recently, atomic layers of WS_2 have also been grown on sapphire (0001) substrates using an LPCVD system, the results of which are depicted in Fig. 5.[20] This growth method is similar to that in Fig. 1c, in that WO_3 powder (contained in a quartz boat) and a target sapphire substrate are successively placed in the hot zone of a furnace. The low-pressure growth conditions, however, are expected to accelerate the volatilization and diffusion of WO_{3-x}, whilst also suppressing the deposition of WO_{3-x}/WS_2 clusters and ensuring uniform nucleation.

The distance between the substrate and the source or precursor (D_{ss}) was found to be a crucial factor in the growth of WS_2 on sapphire. Specifically, if the growth temperature and carrier gas flow remain constant, then a large size of WS_2 made up of a few layers with rough edges is usually obtained with a small D_{ss} value (Figs. 5b, c), whereas a large D_{ss} produces a small domain of rough-edged monolayer flakes (Figs. 5d,e). The thickness distribution and edge morphology were characterized for both instances by AFM height profiles/images, and were reconfirmed by Raman and PL data (Figs. 5f and 5g). This dependence of growth on D_{ss} indicates that the formation

of WS_2 is sensitive to the local concentration of reactive precursors, which is also observed in the case of MX_2 growth on SiO_2/Si.[29,30] This therefore presents a means of controlling the domain size, flake thickness and even coverage of WS_2 growth by simply varying the D_{ss} used.

Temperature also represents an important factor in the CVD growth, with an increase from 880 to 900 °C under a pure Ar flow transforming the rough edges of WS_2 flakes (Fig. 5h) to a saw-toothed state (Fig. 5i) that is indicative of an increase in crystallinity. The domain size of the flakes is also simultaneously increased from several microns to several tens of microns, while still maintaining its monolayer thickness. The growth temperature is therefore considered to largely determine the edge roughness, domain size and crystallinity of WS_2 on sapphire. Moreover, the fact that the saw-toothed structure appears only on some specific orientations indicates a substrate step effect that limits the diffusion of reactive clusters.

The composition of the carrier gas (Ar/H$_2$) also significantly affects the morphology of WS_2, changing from a saw-tooth edged flake to a sharp-edged triangular monolayer when the carrier gas is switched from pure Ar to a mix of Ar and H$_2$ (Fig. 5j). In this situation, the fact that H$_2$ is a more effective reducing agent than sulphur may promote the reduction of WO_3, either directly or through the formation of H$_2$S, thereby creating a more WO_{3-x}-rich environment for WS_2 growth. Increasing the concentration of gaseous growth precursors can also create a transition from diffusion limited growth to attachment limited growth, which encourages the more thermodynamically stable geometry of a regular triangular shape.[32] Thus, the use of a reductive carrier gas like H$_2$ can help mediate the composition and concentration of reactive species in the gas phase, and influence the final modified flake shape.

Even when using a single-crystal sapphire substrate, however, the growth of WS_2 is rarely epitaxial. Instead, polycrystalline WS_2 flakes with a star-like shape are more frequently observed by SEM (Fig. 5k), which correspond to misoriented domains from different lobes. This non-epitaxial nature is considered to result from the relatively weak vdW interaction at the WS_2/sapphire interface, which is insufficient to drive templated growth with aligned domains at the relatively high temperatures required.[33] With prolonged growth, these misaligned domains are patched together through the inevitable formation of grain boundaries (GBs), thus making

the identification of GBs and domain orientations essential to ensuring the growth of large-domain, high-quality MX_2, and

engineering practical device applications.
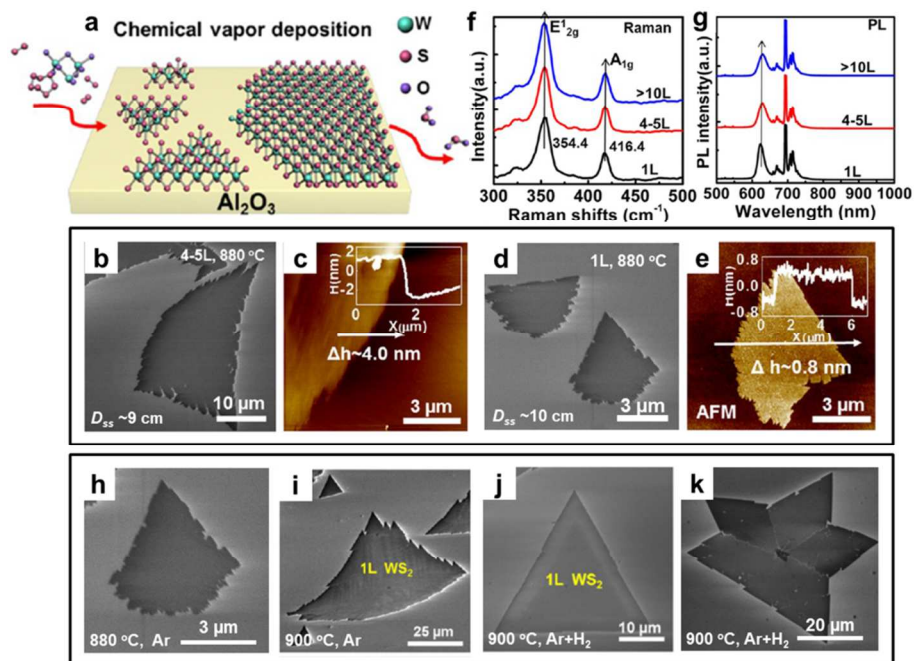
Fig. 5 Engineering the flake morphology of WS_2 synthesized by CVD on a sapphire substrate. (a) Schematic illustration of the growth process.[20] (b, d) SEM images of irregular-edged WS_2 flakes grown on sapphire substrates at 880 °C with a D_{ss} of ~9 cm and 10 cm, respectively.[20] (c, e) Corresponding AFM images for the WS_2 flakes in (d, f).[20] (f, g) Raman and PL spectra for synthesized monolayer and few-layer WS_2 on sapphire.[20] (h) SEM image of a WS_2 flake grown at 880 °C under a pure Ar carrier gas.[20] (i) and (j, k) SEM images of WS_2 flakes grown at 900 °C under pure Ar and $(Ar+H_2)$ carrier gases, respectively.[20] Reproduced with permission from Ref.20. Copyright 2013, American Chemical Society.

The flake morphology of CVD-grown MX_2 can be further modulated using growth substrates that can provide distinct interface interactions with MX_2 adlayers. For example, using a $SrTiO_3(001)$ (STO) substrate at an elevated temperature of 880 °C creates an interesting example of the fractal growth of monolayer MoS_2 (Figs. 6a),[34] with the unique dendritic nature of the MoS_2 flakes (Fig. 6b) being notably different from traditional triangular or polygonal shapes. This is attributed to a strong interfacial interaction between MoS_2 and STO, which is believed to heavily influence the adsorption/desorption and surface diffusion dynamics of precursor species on the substrate. Nevertheless, a nearly continuous patchwork of fractal flakes can still be achieved on STO with a prolonged growth time of 1 h (Fig. 6c), which can then be perfectly transferred onto arbitrary substrates without losing its dendritic morphology (Fig. 6d). Furthermore, this transferred monolayer film (Fig. 6e) is also compatible with flexible substrates such as PET (Fig.

6f), providing a promising option for flexible energy conversion/harvesting and optoelectronic devices.

The dendritic monolayers of MoS_2 typically possess a rather high crystalline quality, as evidenced by a pronounced A-exciton emission at 667.4 nm after being transferred onto SiO_2/Si (Fig. 6g). Moreover, the rough and irregular edge of such flakes is still single crystalline as characterized by the DF-TEM image and corresponding SAED pattern in Figs. 6h and 6i. An interesting potential application of this is the transfer of dendritic MoS_2 onto Au foils to provide an electrocatalyst for the hydrogen evolution reaction (HER) (Fig. 6j), the effectiveness of which is reflected in a low onset potential of ~-0.1 V (Fig. 6k) and a relatively high exchange current density of ~24.5 $\mu A/cm^2$ (Fig. 6l). It is believed that this excellent HER efficiency is directly related to the abundant active edge sites provided by dendritic MoS_2.
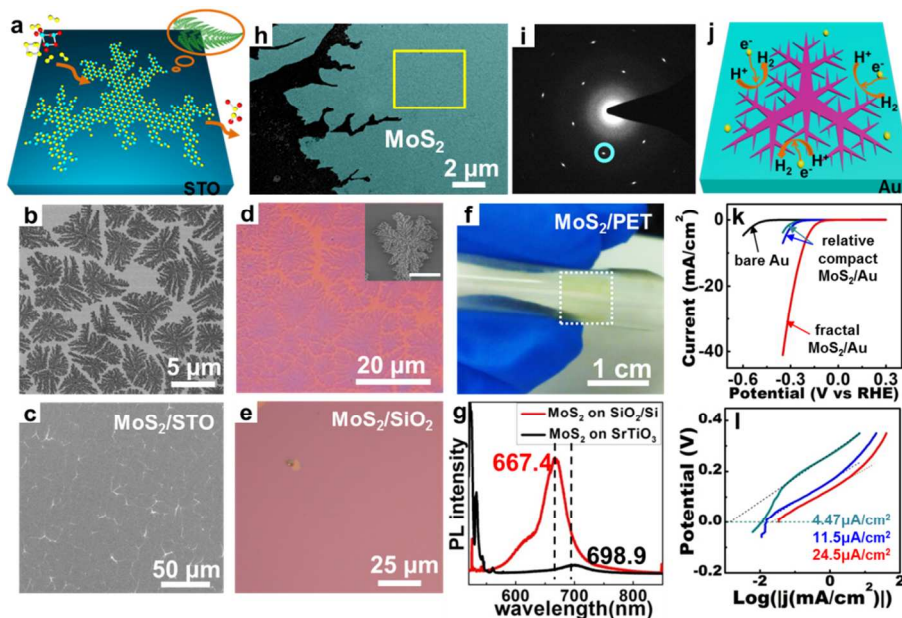
Fig. 6 CVD growth of fractal MoS_2 monolayers on $SrTiO_3$ (001) substrates. (a) Schematic for fractal growth.[34] (b, c) SEM images of dendritic and near-complete monolayer MoS_2 on $SrTiO_3$ substrates.[34] (d, e) Optical images of the MoS_2 films in (b, c) after being transferred onto SiO_2/Si. The inset of (d) is a SEM image of a fractal MoS_2 flake on SiO_2/Si.[34] (f) Transferred monolayer MoS_2 film on a flexible substrate.[34] (g) PL spectra of monolayer MoS_2 before and after transfer.[34] (h) DF-TEM image of the region near the rough edge of a dendritic MoS_2 flake.[34] (i) Corresponding SAED pattern for the highlighted area in (h).[34] (j) Schematic for the HER catalysed by dendritic MoS_2 transferred onto an Au foil.[34] (k) Polarization curves of MoS_2/Au foils.[34] (l) Exchange current densities calculated by applying an extrapolation method to Tafel plots.[34] Reproduced with permission from Ref.34. Copyright 2014, American Chemical Society.

3.2 Grain boundary identification

Aberration-corrected STEM has proven to be an effective way of directly visualising the atomic structure of grain boundaries and the lattice arrangement of adjacent domains.[29,30] Using this technique, various dislocation core structures have been identified at the GBs of CVD MoS_2, including not only a topologically conventional structure with 5- and 7-fold (5|7) rings (Fig. 3g), but also new core structures with (4|4), (4|6), (4|8) and (6|8) fold rings.[35] This diversity is believed to result from the peculiar bonding characteristics between Mo and S in monolayer MoS_2. Nevertheless, the aberration-corrected STEM technique is highly instrument dependent and has an inherently low analysis throughput. As a complimentary technique, DF-TEM presents a way of potentially bridging the gap in scale between the grain and atomic structures of polycrystalline MX_2 (Figs. 3j and 3f).[30]

Photoluminescence mapping of polycrystalline MoS_2 flakes has been used to distinguish embedded GBs from pristine regions (Figs. 7a,b),[30] from which, density functional theory (DFT) calculations have revealed that the reconstruction of GBs has the potential to generate new states near the Fermi level. These are likely to contribute to local doping or strain effects,[30] which would explain the localised modification of the PL signal. However, additional charge disorder effects induced by the underlying substrate and surface adsorbates also need to be considered, which greatly complicates the interpretation of PL mapping results.

The high reactivity of GBs with regards to oxidation or impurity adsorption in ambient atmosphere is schematically presented in Fig. 7c.[20] In experiments involving mild oxidation under moisture-rich conditions, the GBs of intersecting or adjoining flakes (Figs. 7d-f) can be readily visualized by SEM as bright-line shape contrasts (Figs. 7g-i). Through subsequent PL analysis, it was verified that these GBs generally exhibit a greatly reduced PL intensity when compared to pristine regions well away from the GBs (Fig. 7j).

In addition, a new characterization technique known as second harmonic generation (SHG) has been recently introduced for identifying GBs embedded in continuous MoS_2 films (Figs. 7k-n).[36] This allows the few-atom-wide line defects that stitch together different crystal grains to be visualized through destructive interference and annihilation of second-order nonlinear waves from neighbouring atomic domains (Fig. 7l). By analysing the polarised components of this SHG, the crystal orientation of the polycrystalline membrane can be resolved (Figs. 7m, n). In effect, this technique allows for the high-throughput mapping of crystal grains and grain boundaries over large areas with non-invasive all-optical operations.
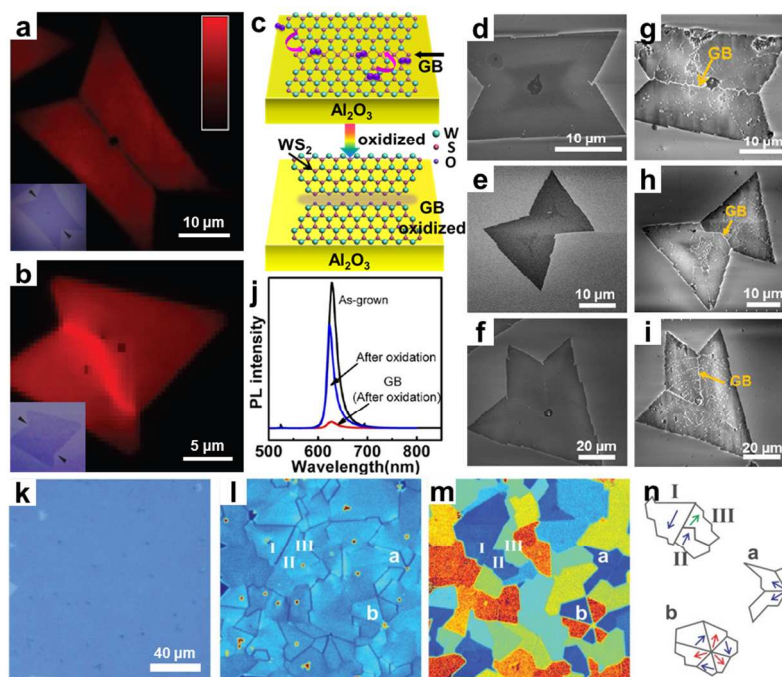
Fig. 7 Imaging the grain boundaries of polycrystalline MX_2 monolayers. (a, b) PL mapping images of polycrystalline MoS_2 with mirror symmetric and faceted tilt grain boundaries, respectively.[30] Reproduced with permission from Ref.30. Copyright 2013, Nature Publishing Group. (c) Schematic model for the surface oxidation of polycrystalline WS_2.[20] (d-f) SEM images of as-grown WS_2 monolayer polygons.[20] (g-i) SEM images of WS_2 grain structures following mild oxidation.[20] (j) PL spectra of samples without and with oxidation (far away from and at the grain boundary).[20] Reproduced with permission from Ref.20. Copyright 2013, American Chemical Society. (k, l) Optical and SHG images, respectively, of a large-area CVD-grown monolayer of MoS_2 on SiO_2/Si.[36] (m) SHG image of the same area as that of (k, l) showing the crystal orientations of irregularly shaped polycrystalline aggregates.[36] (n) Schematic of the area marked in (m), with the arrows indicating domain orientations.[36] Reproduced with permission from Ref.36. Copyright 2014, American Association for the Advancement of Science.

3.3 Domain orientation alignment

Aligning the orientation of individual seeds is an essential step towards large-domain and even wafer-scale single crystal growth of monolayer MX_2, but relies on the defect-free coalescence of these aligned domains. To ensure this is possible, dislocation cores at the merging lines need to have a relatively low formation energy, which is indeed the situation for MX_2 as proven by first principle calculations.[37]

Uniform domain orientation can be achieved through vdW epitaxy of MX_2 on single crystal substrates if two factors are taken into account: a suitable growth temperature and a pronounced rotational anisotropy of the interface binding between MX_2 and the substrate. In this instance, a lower growth temperature is considered beneficial to ensuring better alignment of the MX_2 seeds, as the greater thermal energy (k_BT) at higher growth temperatures (i.e. >800 °C) encourages a more random orientation.[20] Meanwhile, the lattice registry between the MX_2 overlayer and underlying substrate can induce particular commensurate configurations conducive to the rotational alignment of MX_2 domains, in much the same way as the aligned growth of graphene on Ge(110) substrates.[38]

Our group has previously reported on the suitability of fluorophlogopite mica ($KMg_3AlSi_3O_{10}F_2$) as a substrate for the

vdW epitaxial growth of monolayer MoS_2 (Fig. 8),[24] the premise of which lies in the perfect lattice matching of MoS_2 and mica (a(mica)/a(MoS_2)~√3, upper panel in Fig. 8a). A much lower growth temperature of ~530 °C, as compared to previous growth systems (around 800 °C), was adopted during the CVD process,[24] and by varying the source-substrate distance and growth time, monolayer MoS_2 flakes with tunable coverage and domain sizes were achieved (Figs. 7b-d). The uniform spatial distribution (Figs. 8b-d) and similarity in domain size (Fig. 8e) of the triangular MoS_2 seeds in each SEM image indicate a homogeneous nucleation process over the entirety of the mica substrate. The seeds were also found to align primarily along two orientations, representing triangles rotated by 180°, as highlighted by the dashed rhombus in Fig. 8b. This preferential orientation has been further substantiated by detailed orientation statistics (Fig. 8f), which show two narrow peaks at 22° and 38°.

The growth of MoS_2 on mica provides a good demonstration of the unique traits of homogeneous nucleation and preferred domain orientation. These results differ from those of MX_2 on SiO_2/Si with inhomogeneous nucleation (Fig. 3d), in which non-uniform domain sizes (Figs. 4a, i) and random domain orientations (Fig. 8g) were prevalent.[18,29] The CVD growth of MoS_2 on mica is therefore considered to follow

a unique vdW epitaxial mode, and under moderate growth temperatures, there is a high likelihood of MoS$_2$ domains being aligned to substrates with a matching lattice structure.
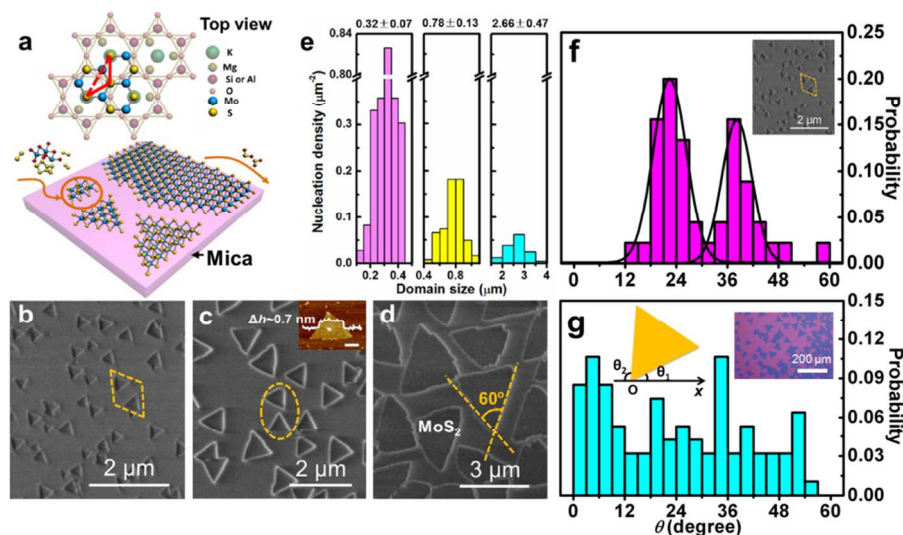

Fig. 8 Epitaxial growth of monolayer MoS$_2$ on lattice-matching mica substrates. (a) A schematic view illustrating the surface reaction during epitaxial growth of MoS$_2$. The upper panel gives the probable occupation of MoS$_2$ on mica.[24] (b−d) SEM images showing the initial growth of MoS$_2$ on mica. Inset in (c) is the AFM profile of the MoS$_2$ flake (scale bar 200 nm).[24] (e) Statistical relation between the surface nucleation density and flake size obtained from the samples shown in b−d (corresponding to left to right); numbers given above the graphs are the average flake size.[24] Reproduced with permission from Ref.24. Copyright 2013, American Chemical Society. (f) Orientation statistics of the MoS$_2$ triangles in (b). The black lines are Gaussian fitting curves. (g) Orientation statistics of triangular MoS$_2$ flakes grown on SiO$_2$/Si, which are based on the inset optical image in Fig. 4a. The orientation angle (θ), as defined as the smaller of the two angles (θ_1 and θ_2) and calculated from the orientations of the lower two edges relative to the horizontal direction, respectively.

3.4 Thickness uniformity

The unique epitaxial growth mechanism of MoS$_2$ can potentially be utilized to synthesize films with superior uniformity in thickness. Indeed, the in-plane coalescence of aligned MoS$_2$ seeds may actually be energetically preferable due to the elimination of dangling bonds at edge sites (Fig. 9a). Thus, prolonged epitaxial growth of MoS$_2$ on mica gives rise to an in-plane merging of micro-sized domains into a continuous film (Fig. 9b).[24] SEM and AFM images (Figs. 9c, d) of a quasi-continuous MoS$_2$ monolayer substantiate the notion that in-plane coalescence is preferred over interlayer overlapping at the merging interfaces. The resulting MoS$_2$ film therefore exhibits superior monolayer uniformity, as verified by the homogeneous intensities of its Raman (Figs. 9e, f) and PL (Figs. 9g, h) mapping images over lengths of tens of microns.

This large-scale monolayer uniformity, which is further confirmed by its uniform optical contrast after being transferred onto SiO$_2$/Si (Fig. 9i), indicates that the growth of MoS$_2$ is influenced by the exposed mica surface via a surface-limited growth mechanism.[44] It is therefore believed that the relatively low interfacial free energy of MoS$_2$/mica contributes to the 2D growth, leading to macroscopically uniform MoS$_2$ films with a strict monolayer thickness (inset in Fig. 9b).[24] Significantly, the low growth temperature of 530 °C doesn't appear to degrade the crystal quality of the MoS$_2$ film in any way, as illustrated by the perfect atomic lattices imaged by TEM (Figs. 9j, k).

It is therefore surmised that not only has vdW epitaxial growth of monolayer MoS$_2$ been achieved on lattice-matching mica substrates at moderate temperatures (530 °C), but that this allows for the alignment and in-plane coalescence of individual MoS$_2$ seeds into high-quality MoS$_2$ films that are strictly monolayer and possess centimetre-scale uniformity.
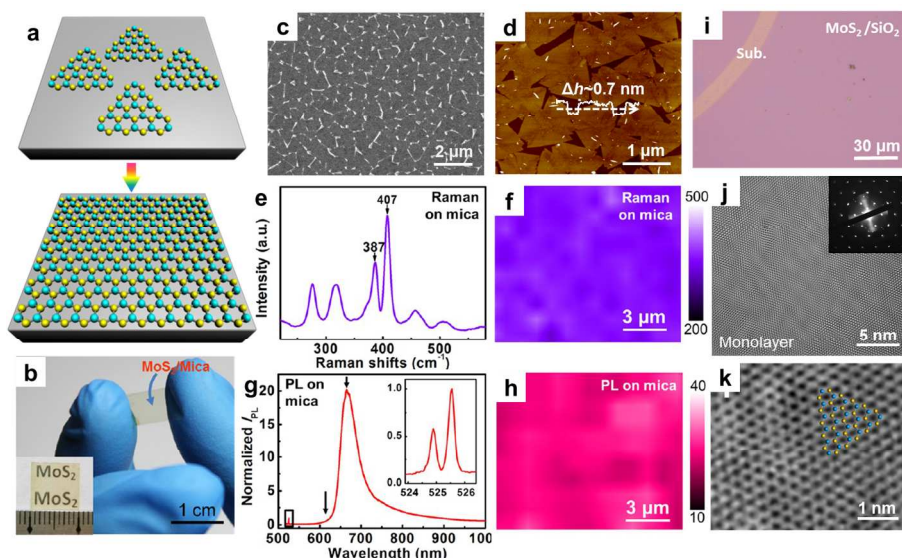
Fig. 9 In-plane continuity and thickness uniformity of epitaxial monolayer MoS_2 grown on mica. (a) Schematic depicting the growth of a continuous MoS_2 film through the coalescence of aligned MoS_2 domains. (b) Photograph of a full-coverage MoS_2 monolayer grown on mica.[24] (c, d) SEM and AFM images, respectively, of a nearly full-coverage MoS_2 layer on mica.[24] (e, g) Raman and PL spectra of an epitaxial MoS_2 monolayer on mica.[24] (f, h) Raman and PL intensity mapping images, respectively, of a ~10 × 10 μm^2 area.[24] (i) Optical image of a MoS_2 monolayer after being transferred onto SiO_2/Si.[24] (j) Atomic-resolution TEM image of a monolayer MoS_2 film. The corresponding SAED pattern collected within a 500× 500 nm^2 area is shown in the top right.[24] (k) zoomed-in image of (j).[24] Reproduced with permission from Ref.24. Copyright 2013, American Chemical Society.

4. Crystal quality evaluation

Having described in detail the CVD growth of MX_2 atomic layers in the preceding sections, it is important now to also consider the crystalline quality of such films. This is typically accomplished by using PL spectroscopy to identify the direct-bandgap nature of monolayer MX_2, and so a strong PL emission is considered to correlate with a high crystal quality. However, recent investigation has revealed that a strong PL enhancement can be obtained in MoS_2 through defect engineering and oxygen bonding.[40] This finding goes a long way to explaining why a CVD-synthesized monolayer of MoS_2 often presents a stronger PL emission but lower carrier mobility, than its exfoliated counterparts.
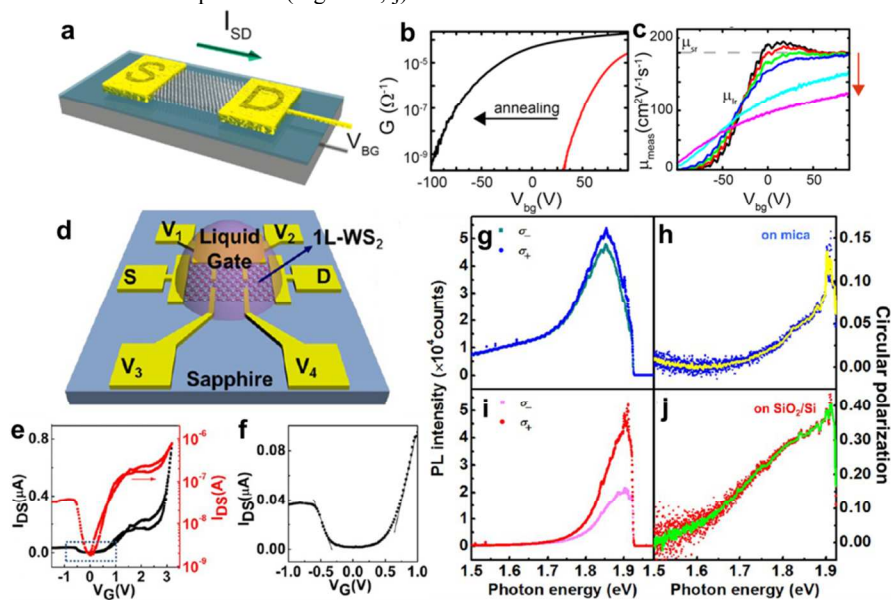
Electrical measurement is a more reliable method to evaluate the crystal quality of monolayer MX_2, especially given the minor contact resistance at the interface between it and metal electrode. Moreover, since MX_2 atomic layers are usually grown on SiO_2/Si substrates, such samples are generally amenable to fabrication of conventional backgated field-effect transistors (FETs) (schematic in Fig. 10a). Using just such a device configuration, Eda et al. reported that CVD-synthesized monolayer MoS_2 exhibits a pronounced n-type behaviour with a threshold voltage of less than -50 V (Fig. 10b).[41] This heavy doping effect was largely attributed to the substantial charge traps created by the amorphous SiO_2/Si substrate.[42] Nevertheless, the estimated room-temperature electron mobility can be as high as ~45 $cm^2V^{-1}s^{-1}$, which is suggestive of a crystal quality comparable with that of mechanically exfoliated monolayers.[9] Moreover, low-temperature measurements revealed an upper-limit mobility of ~200 $cm^2V^{-1}s^{-1}$ for MoS_2 monolayers (Fig. 10c), which is still well below the acoustic-phonon-limited mobility predicted by theory.[43] On the basis of this, it is considered that the samples in question must have contained numerous structural defects, which would contribute to the short-range scattering and dominate the carrier conduction at low temperature.

Since MoS_2 monolayers that are synthesized on SiO_2/Si by CVD are often heavily electron doped, it can be difficult to assess the ambipolar conduction regime with backgate configurations. However, in-situ electrical measurements of as-grown monolayer WS_2 on sapphire with an ionic liquid gate (Fig. 10d) have revealed a relatively low intrinsic doping level (Fig. 10e) and an ambipolar transfer behaviour (Fig. 10f).[20] A similar observation has also been made in the case of monolayer WSe_2 grown on sapphire,[23] suggesting that insulating single crystal substrates have fewer disordered charge traps on their uniform surface, thus rendering a low doping level and high electronic quality in MX_2 overlayers.

Particularly, a unique spectroscopic technique, namely helicity resolved PL spectroscopy, can also be used to assess the crystal quality of MoS_2 monolayers (Figs. 10g-j).[44] Using this method, nonequivalent valleys centred at K and K' points in the momentum space are selectively excited with left- and right-handed lights, respectively,[8] and subsequent radiative relaxation emits light with the same helicity. However, the presence of structural defects greatly enhances the intervalley scattering and rebalances the valley-polarized photocarriers, thereby strongly suppressing the PL helicity (defined as $P(\sigma_+) = \frac{I(\sigma_+)-I(\sigma_-)}{I(\sigma_+)-I(\sigma_-)}$ with σ_+ excitation, where $I(\sigma_\pm)$ denotes the PL intensity of the right (left)-handed component). Consequently, PL helicity can serve as a sensitive indicator for the crystal quality of monolayer MoS_2.

In the case of epitaxially grown MoS_2 monolayers on mica, the room-temperature $P(\sigma_+)$ shows a peak value of only ~0.1 (Figs. 10g, h), which is most likely caused by a scattering of interface charge traps. However, after being transferred onto a fresh SiO_2/Si substrate, the $P(\sigma_+)$ increases up to ~0.35 at room-temperature (Figs. 10i, j).[24]

which is a comparable value to that of high-quality exfoliated monolayer samples.[45] Helicity resolved PL measurement therefore confirms that CVD synthesized MX_2 monolayers can indeed present equivalent crystal quality to that of their exfoliated counterparts.

Fig. 10 Electrical and valley-related properties of a MX_2 monolayer. (a) Schematic diagram of a two-terminal field effect device fabricated on CVD-grown MoS_2 crystallites.[41] (b) Gate dependence of conductance before (red) and after (black) in-situ annealing under vacuum, as measured at 10 K.[41] (c) Mobility as a function of gate voltage. Temperatures are 10, 20, 30, 40, 100, and 150 K (the red arrow points toward higher temperatures).[41] Reproduced with permission from Ref.41. Copyright 2014, American Chemical Society. (d) Schematic illustration of an ionic-liquid-gated FET fabricated using as-grown monolayer WS_2 on sapphire.[20] (e) Transfer curve of the FET and (f) Zoomed-in plot of the dashed rectangle region in (e).[20] Reproduced with permission from Ref.20. Copyright 2013, American Chemical Society. (g, i) Helicity-resolved PL spectra of monolayer MoS_2 as-grown on mica and after being transferred onto SiO_2/Si, respectively.[24] (h, j) Circular polarization of the PL signals corresponding to (g, i).[24] Reproduced with permission from Ref.24. Copyright 2013, American Chemical Society.

5. Beyond MX_2 monolayers: alloying

The alloying of semiconductors with different bandgaps has been widely used in the bandgap engineering of bulk semiconductors, and thus the atomic-level aspects of this alloying phenomenon are of great scientific interest for 2D materials. In particular, there are a number of nanoelectronic and nanophotonic applications that require a tunable spectral response, creating an urgent need to develop 2D semiconducting nanomaterials with continuously tunable bandgaps. Insofar as the bandgap of MX_2 monolayers is concerned, their structural similarity has enabled a uniform atomic mixing of different MX_2 materials within a strictly defined 2D plane. This section therefore focuses on the recent advances that have been made in the CVD synthesis of monolayer MX_2 alloys.

The CVD synthesis of ternary $MoS_{2(1-x)}Se_{2x}$ nanosheets with tunable compositions (Figs. 11a-c) has been achieved by Duan et al.[46] using a methodology very similar to that depicted in Fig. 3a. The notable difference was that two chalcogen powders (selenium and sulphur) were placed at upstream, with a temperature gradient along the quartz tube then applied to enable control over the composition and spatial separation (Fig. 11b). Thus, by simply

changing the position of the boat filled with MoO_3 and the SiO_2/Si substrate above, the constituent stoichiometries of the resulting nanosheets can be elegantly varied from pure MoS_2 to an intermediate $MoS_{2(1-x)}Se_{2x}$, and even as far as pure $MoSe_2$. Normalized PL spectra collected from $MoS_{2(1-x)}Se_{2x}$ nanosheets grown in this way at between 830 and 796 °C exhibit a fully tunable band edge emission from 668 nm (for pure MoS_2) to 795 nm (for pure $MoSe_2$) (Fig. 11c). This spectral result demonstrates the viability of synthesizing MX_2 nanosheet alloys.

Xie et al. have also reported on the physical vapour deposition (PVD) of monolayer $MoS_{2(1-x)}Se_{2x}$ through the direct evaporation of $MoSe_2$ and MoS_2 powders at high temperatures of ~950 °C, followed by downstream alloying at ~650 °C (upper panel in Fig. 11d).[47] Using this method, uniformly distributed monolayer $MoS_{2(1-x)}Se_{2x}$ triangle flakes (lower panel in Fig. 11d), and even continuous films, were synthesized on SiO_2/Si substrates. The x value could also be finely tuned by varying the evaporation temperature of $MoSe_2$ within a range of 940–975 °C, while keeping the evaporation temperature of MoS_2 at 940 °C. High-angle annular dark-field (HAADF) STEM imaging of the S and Se distribution at an atomic level produced a Z-contrast resolved

image (Fig. 11e) that demonstrates the different X_2 sites ($X_2=S_2$, SSe, Se_2), and reveals the distribution of Mo coordination configurations ($M(X_2)_3$) agreeing well with theoretically predicted binomial distribution (Fig. 11f), This result indicates a random arrangement of S and Se around Mo atoms,

corresponding to a perfect alloying. Other synthesis methods for alloying MX_2 include post-growth chalcogen exchange[48] and chemical vapour transport,[49] but are not described here due to space limitations.
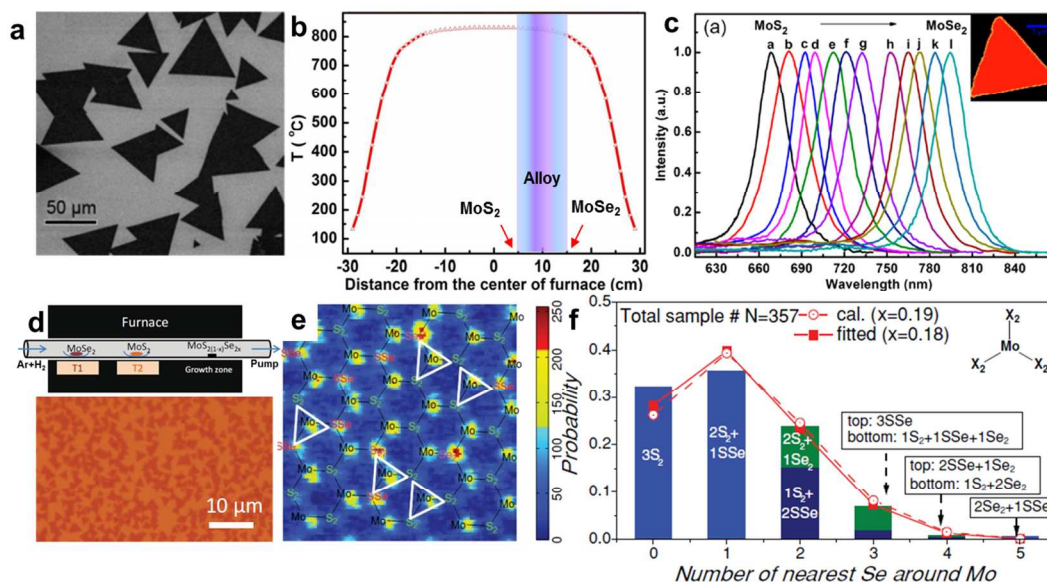
Fig. 11 Preparation of monolayer MX_2 alloys. (a) Typical SEM morphology of ternary $MoS_{2(1-x)}Se_{2x}$ nanosheets.[46] (b) Growth window for achieving ternary $MoS_{2(1-x)}Se_{2x}$ nanosheets.[46] (c) PL spectra of $MoS_{2(1-x)}Se_{2x}$ nanosheets with a tunable x value.[46] Reproduced with permission from Ref.46. Copyright 2014, American Chemical Society. (d) Upper panel: schematic of the PVD system used to grow $MoS_{2(1-x)}Se_{2x}$ monolayer alloy. Lower panel: optical image of as-grown $MoS_{1.60}Se_{0.40}$ triangles.[47] (e) False-colour HAADF-STEM image. Mo sites: yellow; S_2 sites: light blue; SSe sites: yellow, and Se_2 sites: red.[47] (f) Probability of finding different coordination configurations.[47] The open circles are the calculated probability using a binomial distribution with an x value of 0.19. The solid squares are fitted experimental values. Reproduced with permission from Ref.47. Copyright 2014, John Wiley & Sons, Inc.

6. Conclusion and outlook

As the thinnest known semiconductor, monolayer group-VIB transition metal dichalcogenides (MX_2) offer unique physical and chemical properties that give them great potential for use as a host material in future nanoelectronic, optoelectronic, photocatalytic applications. However, their use has so far been limited by a lack of suitable batch production methods capable of achieving large-domain, high-quality MX_2 monolayers. A solution to this problem may lie in the use of CVD, which has proven to be effective for preparing 2D nanomaterials. Two synthesis routes have therefore been proposed for the CVD growth of MX_2 thin films: the sulphurisation/decomposition of pre-deposited metal-based precursor layers into MX_2 (Route 1), and the simultaneous introduction of gas-phase metal oxide and chalcogen precursors for direct reaction into MX_2 (Route 2).

Enlarging the domain size is highly desired in the CVD growth of monolayer MX_2, which can be accomplished to some extent by suppressing the nucleation density on a clean SiO_2/Si surface. And preliminary results suggest that using insulating single-crystal substrates instead of amorphous SiO_2/Si can create additional opportunities to engineer the flake morphology, regulate the domain orientation, and achieve

superior thickness uniformity at a macroscopic scale. In particular, defect-free coalescence of aligned MX_2 domains may provide further opportunity in growing wafer-scale single crystals, with the growth mediated by a vdW epitaxy regime. Increasing the crystal quality is another critical issue for the CVD synthesized MX_2, which can be substantiated by a low doping level, high carrier mobility, and high PL helicity at room temperature. An insulating single-crystal substrate owing an atomically uniform and chemically inert surface with fewer charge traps can therefore potentially be used to obtain high quality monolayer MX_2.

Further investigation of monolayer MX_2 should ideally focus on tailoring its band structure through alloying or constructing heterostructures, as this may open up the possibility of engineering it to explore novel physics or create new practical applications. Furthermore, a combination of MX_2 and other 2D nanomaterials, such as semimetallic graphene and insulating h-BN, may help create a new world of 2D materials,[50] in which semiconducting monolayer MX_2 will undoubtedly be one of the essential cornerstones.

Acknowledgements

References

1. K. S. Novoselov, D. Jiang, F. Schedin, T. J. Booth, V. V. Khotkevich, S. V. Morozov and A. K. Geim, *Proc. Natl. Acad. Sci. U. S. A.*, 2005, **102**, 10451-10453.

2. K. S. Novoselov, A. K. Geim, S. V. Morozov, D. Jiang, M. I. Katsnelson, I. V. Grigorieva, S. V. Dubonos and A. A. Firsov, *Nature*, 2005, **438**, 197-200.

3. Q. H. Wang, K. Kalantar-Zadeh, A. Kis, J. N. Coleman and M. S. Strano, *Nat. Nanotechnol.*, 2012, **7**, 699-712.

4. A. Splendiani, L. Sun, Y. Zhang, T. Li, J. Kim, C.-Y. Chim, G. Galli and F. Wang, *Nano Lett.*, 2010, **10**, 1271-1275.

5. L. Britnell, R. M. Ribeiro, A. Eckmann, R. Jalil, B. D. Belle, A. Mishchenko, Y.-J. Kim, R. V. Gorbachev, T. Georgiou and S. V. Morozov, *Science*, 2013, **340**, 1311-1314.

6. G. Eda and S. A. Maier, *ACS Nano*, 2013, **7**, 5660-5665.

7. K. F. Mak, K. He, C. Lee, G. H. Lee, J. Hone, T. F. Heinz and J. Shan, *Nat. Mater.*, 2013, **12**, 207-211.

8. D. Xiao, G.-B. Liu, W. Feng, X. Xu and W. Yao, *Phys. Rev. Lett.*, 2012, **108**, 196802.

9. B. Radisavljevic, A. Radenovic, J. Brivio, V. Giacometti and A. Kis, *Nat. Nanotechnol.*, 2011, **6**, 147-150.

10. G. Eda, H. Yamaguchi, D. Voiry, T. Fujita, M. Chen and M. Chhowalla, *Nano Lett.*, 2011, **11**, 5111-5116.

11. Z. Zeng, Z. Yin, X. Huang, H. Li, Q. He, G. Lu, F. Boey and H. Zhang, *Angew.Chem., Int. Ed.*, 2011, **50**, 11093-11097.

12. J. N. Coleman, M. Lotya, A. O'Neill, S. D. Bergin, P. J. King, U. Khan, K. Young, A. Gaucher, S. De, R. J. Smith, I. V. Shvets, S. K. Arora, G. Stanton, H.-Y. Kim, K. Lee, G. T. Kim, G. S. Duesberg, T. Hallam, J. J. Boland, J. J. Wang, J. F. Donegan, J. C. Grunlan, G. Moriarty, A. Shmeliov, R. J. Nicholls, J. M. Perkins, E. M. Grieveson, K. Theuwissen, D. W. McComb, P. D. Nellist and V. Nicolosi, *Science*, 2011, **331**, 568-571.

13. Y. Zhan, Z. Liu, S. Najmaei, P. M. Ajayan and J. Lou, *Small*, 2012, **8**, 966-971.

14. X. Wang, H. Feng, Y. Wu and L. Jiao, *J. Am. Chem. Soc.*, 2013, **135**, 5304-5307.

15. K.-K. Liu, W. Zhang, Y.-H. Lee, Y.-C. Lin, M.-T. Chang, C.-Y. Su, C.-S. Chang, H. Li, Y. Shi, H. Zhang, C.-S. Lai and L.-J. Li, *Nano Lett.*, 2012, **12**, 1538-1544.

16. Y. H. Lee, X. Q. Zhang, W. Zhang, M. T. Chang, C. T. Lin, K. D. Chang, Y. C. Yu, J. T. W. Wang, C. S. Chang, L.-J. Li and T.-W. Lin, *Adv. Mater.*, 2012, **24**, 2320-2325.

17. Y.-H. Lee, L. Yu, H. Wang, W. Fang, X. Ling, Y. Shi, C.-T. Lin, J.-K. Huang, M.-T. Chang, C.-S. Chang, M. Dresselhaus, T. Palacios, L.-J. Li and J. Kong, *Nano Lett.*, 2013, **13**, 1852-1857.

18. X. Ling, Y.-H. Lee, Y. Lin, W. Fang, L. Yu, M. S. Dresselhaus and J. Kong, *Nano Lett.*, 2014, **14**, 464-472.

19. H. R. Gutiérrez, N. Perea-López, A. L. Elías, A. Berkdemir, B. Wang, R. Lv, F. López-Urías, V. H. Crespi, H. Terrones and M. Terrones, *Nano Lett.*, 2012, **13**, 3447-3454.

20. Y. Zhang, Y. Zhang, Q. Ji, J. Ju, H. Yuan, J. Shi, T. Gao, D. Ma, M. Liu, Y. Chen, X. Song, H. Y. Hwang, Y. Cui and Z. Liu, *ACS Nano*, 2013, **7**, 8963-8971.

21. D. Kong, H. Wang, J. J. Cha, M. Pasta, K. J. Koski, J. Yao and Y. Cui, *Nano Lett.*, 2013, **13**, 1341-1347.

22. X. Lu, M. I. B. Utama, J. Lin, X. Gong, J. Zhang, Y. Zhao, S. T. Pantelides, J. Wang, Z. Dong, Z. Liu, W. Zhou and Q. Xiong, *Nano Lett.*, 2014, **14**, 2419-2425.

23. J.-K. Huang, J. Pu, C.-L. Hsu, M.-H. Chiu, Z.-Y. Juang, Y.-H. Chang, W.-H. Chang, Y. Iwasa, T. Takenobu and L.-J. Li, *ACS Nano*, 2013, **8**, 923-930.

24. Q. Ji, Y. Zhang, T. Gao, Y. Zhang, D. Ma, M. Liu, Y. Chen, X. Qiao, P.-H. Tan, M. Kan, J. Feng, Q. Sun and Z. Liu, *Nano Lett.*, 2013, **13**, 3870-3877.

25. Y. Yu, C. Li, Y. Liu, L. Su, Y. Zhang and L. Cao, *Sci. Rep.*, 2013, **3**, 1866.

26. Y. Feldman, E. Wasserman, D. J. Srolovitz and R. Tenne, *Science*, 1995, **267**, 222-225.

27. A. Zak, Y. Feldman, V. Alperovich, R. Rosentsveig and R. Tenne, *J. Am. Chem. Soc.*, 2000, **122**, 11108-11116.

28. Y.-C. Lin, W. Zhang, J.-K. Huang, K.-K. Liu, Y.-H. Lee, C.-T. Liang, C.-W. Chu and L.-J. Li, *Nanoscale*, 2012, **4**, 6637-6641.

29. S. Najmaei, Z. Liu, W. Zhou, X. Zou, G. Shi, S. Lei, B. I. Yakobson, J.-C. Idrobo, P. M. Ajayan and J. Lou, *Nat. Mater.*, 2013, **12**, 754-759.

30. A. M. van der Zande, P. Y. Huang, D. A. Chenet, T. C. Berkelbach, Y. You, G.-H. Lee, T. F. Heinz, D. R. Reichman, D. A. Muller and J. C. Hone, *Nat. Mater.*, 2013, **12**, 554-561.

31. C. Cong, J. Shang, X. Wu, B. Cao, N. Peimyoo, C. Qiu, L. Sun and T. Yu, *Adv. Opt. Mater.*, 2014, **2**, 131-136.

32. J. V. Lauritsen, J. Kibsgaard, S. Helveg, H. Topsøe, B. S. Clausen, E. Lægsgaard and F. Besenbacher, *Nat. Nanotechnol.*, 2007, **2**, 53-58.

33. A. Koma, *J. Cryst. Growth*, 1999, **201**, 236-241.

34. Y. Zhang, Q. Ji, G.-F. Han, J. Ju, J. Shi, D. Ma, J. Sun, Y. Zhang, M. Li, X.-Y. Lang, Y. Zhang and Z. Liu, *ACS Nano*, 2014, **8**, 8617-8624.

35. W. Zhou, X. Zou, S. Najmaei, Z. Liu, Y. Shi, J. Kong, J. Lou, P. M. Ajayan, B. I. Yakobson and J.-C. Idrobo, *Nano Lett.*, 2013, **13**, 2615-2622.

36. X. Yin, Z. Ye, D. A. Chenet, Y. Ye, K. O'Brien, J. C. Hone and X. Zhang, *Science*, 2014, **344**, 488-490.

37. X. Zou, Y. Liu and B. I. Yakobson, *Nano Lett.*, 2012, **13**, 253-258.

38. J.-H. Lee, E. K. Lee, W.-J. Joo, Y. Jang, B.-S. Kim, J. Y. Lim, S.-H. Choi, S. J. Ahn, J. R. Ahn and M.-H. Park, *Science*, 2014, **344**, 286-289.

39. X. Li, W. Cai, J. An, S. Kim, J. Nah, D. Yang, R. Piner, A. Velamakanni, I. Jung, E. Tutuc, S. K. Banerjee, L. Colombo and R. S. Ruoff, *Science*, 2009, **324**, 1312-1314.

40. H. Nan, Z. Wang, W. Wang, Z. Liang, Y. Lu, Q. Chen, D. He, P. Tan, F. Miao, X. Wang, J. Wang and Z. Ni, *ACS Nano*, 2014, **8**, 5738-5745.

41. H. Schmidt, S. Wang, L. Chu, M. Toh, R. Kumar, W. Zhao, A. H. Castro Neto, J. Martin, S. Adam, B. Özyilmaz and G. Eda, *Nano Lett.*, 2014, **14**, 1909-1913.

42. S. Ghatak, A. N. Pal and A. Ghosh, *ACS Nano*, 2011, **5**, 7707-7712.

43. K. Kaasbjerg, K. S. Thygesen and K. W. Jacobsen, *Phys. Rev. B*, 2012, **85**, 115317.

44 H. Zeng, J. Dai, W. Yao, D. Xiao and X. Cui, *Nat. Nanotechnol.*, 2012, **7**, 490-493.

45 G. Sallen, L. Bouet, X. Marie, G. Wang, C. R. Zhu, W. P. Han, Y. Lu, P. H. Tan, T. Amand, B. L. Liu and B. Urbaszek, *Phys. Rev. B*, 2012, **86**, 081301.

46 H. Li, X. Duan, X. Wu, X. Zhuang, H. Zhou, Q. Zhang, X. Zhu, W. Hu, P. Ren, P. Guo, L. Ma, X. Fan, X. Wang, J. Xu, A. Pan and X. Duan, *J. Am. Chem. Soc.*, 2014, **136**, 3756-3759.

47 Q. Feng, Y. Zhu, J. Hong, M. Zhang, W. Duan, N. Mao, J. Wu, H. Xu, F. Dong, F. Lin, C. Jin, C. Wang, J. Zhang and L. Xie, *Adv. Mater.*, 2014, **26**, 2648-2653.

48 Q. Ma, M. Isarraraz, C. S. Wang, E. Preciado, V. Klee, S. Bobek, K. Yamaguchi, E. Li, P. M. Odenthal, A. Nguyen, D. Barroso, D. Sun, G. von Son Palacio, M. Gomez, A. Nguyen, D. Le, G. Pawin, J. Mann, T. F. Heinz, T. S. Rahman and L. Bartels, *ACS Nano*, 2014, **8**, 4672-4677.

49 D. O. Dumcenco, H. Kobayashi, Z. Liu, Y.-S. Huang and K. Suenaga, *Nat. Commun.*, 2013, **4**, 1351.

50 A. K. Geim and I. V. Grigorieva, *Nature*, 2013, **499**, 419-425.